scientific reports

Check for updates

OPEN

Comprehensive study of rapid capacity fade in prismatic Li-ion cells with flexible packaging

Zuzana Stravova[1,7], Ondrej Klvac[2,3,7], Jiri Bana[2,7], Bihag Anothumakkool[4], Tomas Zikmund[1]✉, Pavel Blazek[1,6], Jozef Kaiser[1,5] & Tomas Kazda[2]

Prismatic lithium-ion batteries (LIBs) are considered promising electric energy sources in electromobility applications due to their efficient space utilization. However, their sensitivity to external and internal influences and reduced durability lead to inflation risk and potential explosions throughout their lifecycle. These critical processes are strongly influenced by the inner construction of the cell, especially concerning the coating and mechanical fixation. This study subjects a commercially available prismatic LIB cell to comprehensive, correlative analysis employing various imaging techniques. The inner structure of the entire cell is visualized non-destructively by X-ray computed tomography (CT), enabling the identification of critical design flaws prior to electrochemical cycling. Electrochemical cycling simulates the battery lifecycle, and the cell is subsequently disassembled in the fully charged state. The usage of the inert-gas transfer system allowed the preparation of Broad Ion Beam (BIB) electrodes cross-sections in a fully native state and for the first time to observe the tearing of graphite particles due to over-lithiation. Established region labeling system allowed to use CT and scanning electron microscopy (SEM) correlatively to identify critical regions. After 100 cycles, a 40% capacity loss was observed and event diagram describing deagradation mechanisms, related both to the cell design and to the processes occurring at high load, was created.

Keywords Lithium-ion battery, Prismatic cell, Lithium plating, X-ray computed tomography, SEM

LIBs are currently the only option for powering electrical vehicles (EV) and are expected to remain so in the foreseeable future[1]. In 2019, the total production capacity of LIBs for EVs was 120 GWh, while in 2022, it increased to 250 GWh and is expected to grow further to 1.525 TWh by 2030[1]. According to a European Union report, the transportation segment is responsible for nearly 28% of global carbon dioxide (CO2) emissions, making the shift towards EVs and the development of LIBs crucial[2]. Improving battery performance requires precise knowledge of the structure-composition properties. Analytical techniques are used to provide more information for the development. Battery cells are the fundamental building blocks of LIBs. Currently, three types are used for EV applications: cylindrical, pouch, and prismatic cells [3].

The most used cylindrical cells feature internal components wound around a joint spine[4]. The benefits of this design include dimensional stability during charging and easy integration into a battery pack. However, the battery wiring and management system (BMS) are more complex than other cell types. The battery pack allows good heat dissipation, but there is no good use of space[3].

Pouch and prismatic cells are classed as flat-type cells. Electrodes of pouch cells are layered in a sandwich structure sealed in flexible foil[5]. Pouch cells are usually enclosed in flexible, form-unstable pouch foil serving as a case. It usually consists of an aluminum foil core with non-conductive polymer compound outer layers. The construction of prismatic cells follows a similar design principle to cylindrical cells, but the winding pattern differs in shape due to its elliptical character resembling a pouch cell. Cylindrical and prismatic cells are typically coated with a solid hard case made from aluminium or stainless steel. It may expose the electrodes of prismatic cells to uneven pressure distribution. To mitigate this issue partially, solid material is sometimes employed to fill the corners. However, the inexpensive prismatic cells use housing with the same flexible foil as pouch cells. The

[1]Central European Institute of Technology, Brno University of Technology, Brno, Czech Republic. [2]Department of Electrical and Electronic Technology, Faculty of Electrical Engineering and Communication, BUT, Technická 10, Brno 616 00, Czech Republic. [3]Thermo Fisher Scientific, Vlastimila Pecha 12, Brno 627 00, Czech Republic. [4]Thermo Fisher Scientific, Achtseweg Noord 5, Eindhoven 5651 GG, The Netherlands. [5]Institute of Physical Engineering, Faculty of Mechanical Engineering, Brno University of Technology, Brno, Czech Republic. [6]WZL | RWTH Aachen University, Aachen, Germany. [7]These authors contributed equally: Zuzana Stravova and Ondrej Klvac. ✉email: Tomas.Zikmund@ceitec.vutbr.cz

advantage of using flexible foil includes weight reduction; meanwhile, the disadvantage includes functionality problems during their operation—prismatic cells using flexible foil as housing are subjected to investigation within this work[5,6].

The primary benefit of prismatic cells compared to the other types of cells is in the energy density per mass, making them suitable solutions for heavy vehicles like buses and trucks. However, expensive manufacturing and faster ageing are the main downfalls. The future applications of prismatic cells rely on reducing production costs by producing larger formats than cylindrical cells and thus reducing the cost per cell[7]. Northvolt is constructing a factory in Norway dedicated to producing prismatic cells, which will be 2024 the largest LIB factory in Europe with an annual capacity of 60 GWh[8]. Further investigation is necessary to avoid the rapid capacity degradation and potentially hazardous conditions in prismatic-type LIBs. Additionally, faulty components emerge within the LIBs production process, creating the need to implement reliable methods for detecting such instances.

LIBs undergo various electrical and chemical reactions, phase transformations, volume changes, active material delamination, grains cracking, and solid electrolyte interphase (SEI) over their operation and lifetime. Also, lithium (Li) metal plating on the anode surface is one of the most significant causes of LIB safety issues. It can form dendrites associated with the risk of internal short-circuit. The deposited metallic Li quickly reacts with the electrolyte, which on the one hand, consumes the active Li and electrolyte, and on the other hand, causes the loss of electrical contact of the anode part of the deposited Li accelerating the capacity fade[9]. Due to side reactions of the electrolyte, gas development and cell inflation can also occur. Cells can be stacked and incorporated into a solid plate to limit expansion[10].

It is essential to understand the degradation processes to characterize LIBs and propose changes in their design to achieve higher energy capacity and reliability. Typically used non-destructive methods, allowing for observation of the internal parts without disassembly, are electrochemical techniques such as Galvanostatic Cycling with Potential Limitation (GCPL), Constant Current followed by Constant Voltage (CCCV), Cyclic Voltammetry (CV), and electrochemical impedance spectroscopy (EIS), or X-ray techniques such as Computed Tomography (CT). Following these analyses, the cell remains functional. The methods prove to be suitable, particularly in evaluating the safety aspects of the cell for implementation in secondary storage systems.

CT enables to gain information about inner structure of LIB non-destructively resulting in the 3D digital greyscale representation[11]. In the research of Li-ion batteries, CT allows access to data on various scales, from the analysis of the whole scale level down to the microstructure of electrodes[12]. There are multiple described applications of CT analysis to investigate the ageing process for commercially available cells. Much research has been done to study the 3D morphological evolution of electrodes on a microstructural level during cycling. In these experiments, resolution down to the nanoscale is reached on a small portion of the electrode[13–16]. Studies on the microstructural level broaden the knowledge of active material. However, they are constrained regarding the knowledge of cell architecture evolution with lower resolution, which is necessary when expanding the research regarding new manufacturing methods or preventing structural defects. Research on the whole cell level provides information about electrode deformation or delamination of active material connected to its loss of capacity during ageing. Numerous works have studied the ageing effect on 18,650 Li-ion cells, focusing on inhomogeneous swelling of the jelly-roll electrode windings[17–19]. Blazek et al.[20] focused on expanding the possibilities for higher resolution down to 8 µm on the whole cell level by using helical trajectory micro-CT coupled with virtual unrolling to describe the process of electrode stack swelling. A similar resolution is not achieved with flat-type cells due to their irregular shape, which presents a challenge for CT analysis acquisition. Bond et al.[21] studied the effect of long-term cycling on the morphological changes inside the unmodified pouch cells, leading to extensive microcracking and morphological changes in the cathode. The resolution reached was 9 µm on the whole cell level.

In contrast to possibilities of CT analysis, ex-situ techniques are performed destructively post-mortem but usually provide better resolution and greater detail. These include Scanning and Transmission Electron Microscopy (SEM and TEM) together with Energy Dispersive Spectroscopy (EDS), Atomic Force Microscopy (AFM), or X-ray Diffraction Spectroscopy (XRD). However, in the case of laboratory-assembled cells, the techniques can also be used for in-situ experiments. The subjects of post-mortem analysis are typically individual internal materials – cathode, anode, and separator. Before the cell's disassembly, some X-ray techniques can be performed to provide information about the inner structure of the cell.

SEM is a widely used method for study due to its high resolution. It provides high-magnification images of the microstructure of different materials[22], which enables the observation of the evolution of the surface of electrode particles after ageing[23,24]. SEM is complemented by techniques such as EDS to obtain additional information about the chemical composition. Preparation of high-quality cross-sections before SEM imaging can be supplemented by broad ion beam (BIB) milling[25,26]. However, SEM encounters challenges when studying Li-containing materials. Sample preparation must be carried out in dry boxes or glove boxes under inert gas, as lithium is highly reactive with oxygen, carbon dioxide, nitrogen, and moisture. The analysis is often carried out under ultra-high vacuum or cryogenic conditions to prevent sample reactions during imaging[22].

When disassembling the cell for post-mortem analysis, it is desirable to do so in a deep discharged state to prevent thermal runaway in case of accidental short. However, if the cell voltage falls outside the standard operating window, changes in the material may occur that do not correspond to ageing[27]. Comparison between the new cell stage and aged cell is often conducted to gain a better understanding of structural changes within the ageing process[28]. However, the observation of lithium plating is constrained when disassembling a discharged cell, as this phenomenon is associated with the charging process[29]. Depending on the state of charge (SOC), the colour of the graphite anode changes. Starting from black colour, with an increased amount of intercalated lithium ions, the colour changes to gold for a higher state of charge. When the battery works appropriately, the colour change is homogeneous throughout the anode and is not affected by the depth of the graphite layers[30].

Although it is not usual to disassemble a cell in a charged state for safety reasons, this procedure has the advantage that active and inactive regions can be easily visually identified, as well as the lithium plating process studied.

This work combines several analytical techniques to advance current research on prismatic-type LIBs, emphasising evaluating critical factors such as degree of lithiation, cell swelling, electrode delamination, and defects. The methods are demonstrated on a commercially available prismatic cell and focus on the consequences of suboptimal internal structure design and operation on battery degradation, including electrolyte decomposition, lithium plating on the anode surface, significant cell inflation and capacity loss. These findings offer a valuable correlation between CT imaging and post-mortem BIB milling and SEM analysis. This novel approach presents a benefit for interpreting the CT results of cycled cells.

Subsequently, this work introduces a novel approach allowing the disassembly of LIB cells in a fully charged state, providing insights into the presence of inactive regions resulting from improper construction. By employing a comprehensive, correlative analysis scheme combining CT, an established labelling region system, and an inert gas transfer system between the glovebox, BIB, and SEM, it was possible to prepare high-quality electrode cross-sections in the native state. In this arrangement, it was possible to image the lithium plating on the anode surface and the breakdown of the surface graphite grains on selected regions of interest for the first time. These methods were employed to identify failed components and to propose internal structure design modifications arising from the created event diagram.

Materials and methods

Electrochemical testing

The prismatic cells used for investigation in this work are two commercially available cells from Cellevia Batteries manufacturer, No L402025 (Fig. 1.). The nominal capacity stated in the datasheet is 150 mAh in a total voltage range of 4.20–2.75 V at a current of 0.2 C. The minimum cycle life for these conditions is 500 cycles with a 20% capacity drop as a threshold. The maximum continuous recommended current is 1 C.

The cells were cycled in a four-terminal sensing in an air-conditioned room at a stable temperature of 21 °C using a 16-channel Biologic VMP3 galvanostat/potentiostat in full voltage range in Constant Current followed by Constant Voltage (CCCV) mode – the upper limit has been held for three hours or until the current drops below 7 mA. For analysis performed in this work, two cells were used. The first cell serves as a reference for analyzing the pre-cycling conditions, and the second cell was subjected to cycling. Both cells were initially cycled three times (test cycles) to verify their parameters over a full current range of 0.2 C, 0.5 C and 1.0 C. Subsequently, the reference cell was fully charged and used for the reference state analysis. The second cell was then subjected to full-scale 1 C cycling for 100 cycles, followed by repeated initial three test cycles, then fully charged and disassembled. Impedance spectroscopy was performed under 100% SOC in the 1 MHz – 50 mHz range with 10 mV amplitude before and after full-scale 1 C cycling.

Physical testing

Micro CT analysis

The battery was subjected to imaging using Thermo Scientific HeliScan micro-CT. The system incorporates a 160 kV transmission microfocus tube with a tungsten target and a high-resolution flat-panel detector featuring a resolution of 3072 × 3072 pixels and a pixel size of 139 µm. To capture a high-resolution image of the entire battery in a single scan, a space-filling helical trajectory was employed. This trajectory allowed for optimal positioning of the detector near the X-ray source, resulting in enhanced flux and improved signal-to-noise ratio while effectively avoiding cone beam artefacts, even at a cone angle of 60°. Detailed parameters setting of the micro-CT measurements are listed in the Table 1.

The tomographic reconstruction was realized through the utilization of reconstruction software provided by the system manufacturer. The reconstructed data were further analyzed in VG Studio Max (version 3.4, Volume Graphics GmbH, Germany). To perform the analysis of the internal structure and its defects, both pre-cycling and post cycling following processes were applied:

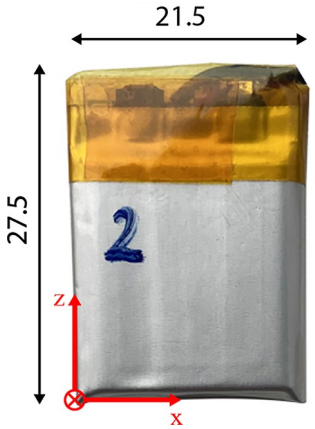


Fig. 1. Cellevia battery L402025; dimensions of the sample and sample orientation in the coordinate system.

Micro-CT measurements parameters	
System	**Thermo Scientific HeliScan**
ROI	Whole cell
Trajectory	Helical
X-ray tube voltage	130 kV
Current	90 µA
Exposure time	2.5 s
Averaged radiographs per projection	3
Projections per Revolution	2880

Table 1. Micro-CT measurements parameters.

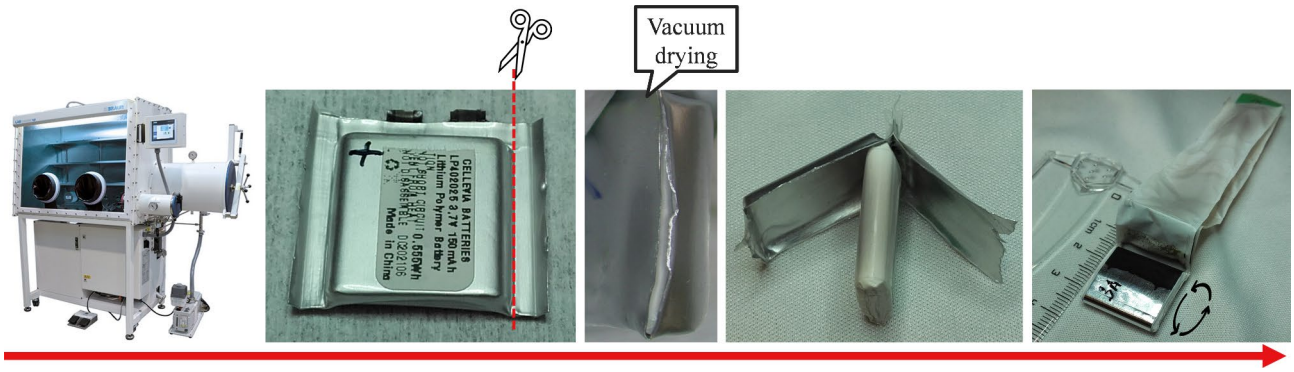


Fig. 2. Battery disassembly procedure described from left to right – the cell is transferred into an Ar-filled glovebox; the cell packaging (case) edge is opened with scissors; the resulting hole (detail) allows the electrolyte evaporation under vacuum in the glovebox antechamber; the whole packaging is removed; the cell is unrolled for separation of individual electrodes.

1. Dataset registration: A simple registration tool was used to align the data to establish the right-handed coordinate system beginning in the bottom left corner of the battery cell.
2. Selection of the tomographic cross-section: The tomographic cross-section at z = 13 mm was selected for further analysis of the layout of the internal structure. The battery pins do not interfere with selected cross-sections allowing for analysis of the central region of the battery cell.
3. A dimensional analysis of the cross-section was performed.

Cell disassembly
Cell disassembly and storage of its parts were performed in an Ar-filled glovebox MBraun with controlled H2O and O2 content < 0.1 ppm (see Fig. 2). First, the welded edges of the cell case were cut with scissors to reveal the internal structure. Subsequently, the cell was placed in the glovebox antechamber and left under vacuum for several minutes to allow most of the electrolyte to evaporate. This reduces contamination of the glovebox and the chance of dangerous accidents as the internal impedance increases significantly. The internal structure is connected to the case by welded metal pins only. Cutting off this part must be done carefully to avoid shorting through the aluminium core of the case. After removing the case, the electrodes were gradually unwound and separately dried in an antechamber for one more hour.

Region labelling scheme To trace specific regions of the battery in micro-CT data, subsequently, to disassembly, it is imperative to establish a region labelling scheme (Fig. 3). These regions are linear segments/layers that are separated by folds, denoted as the cell edge, and are assigned numerical label. The numbering scheme begins at the outermost region and is labelled "1", followed by fold and region "2". The numbering scheme continues in the direction towards the middle of the cell. Furthermore, each region is characterized as well based on its orientation relative to the centre of the cell. Sides facing outward from the centre of the cell are designated as "A", and sides facing inward to the centre of the cell are designated as "B". Labeling is placed on the upper side of the cell, oriented towards the battery pins. The evaluation was conducted inside the glovebox environment utilizing the optical microscope equipped with a camera and LCD screen to facilitate the optical inspection process.

SEM and EDS analysis
SEM imaging and EDS analysis were conducted using a Thermo Scientific Scios 2 instrument with an UltraDry EDS detector. The battery electrodes were analyzed at the surface and cross-section, with sample preparation using Thermo Scientific CleanMill BIB. The instrumentation setup utilizes an adaptation to the Thermo Scientific CleanConnect Sample Transfer System, which enables the transfer of air-sensitive samples between the glovebox,

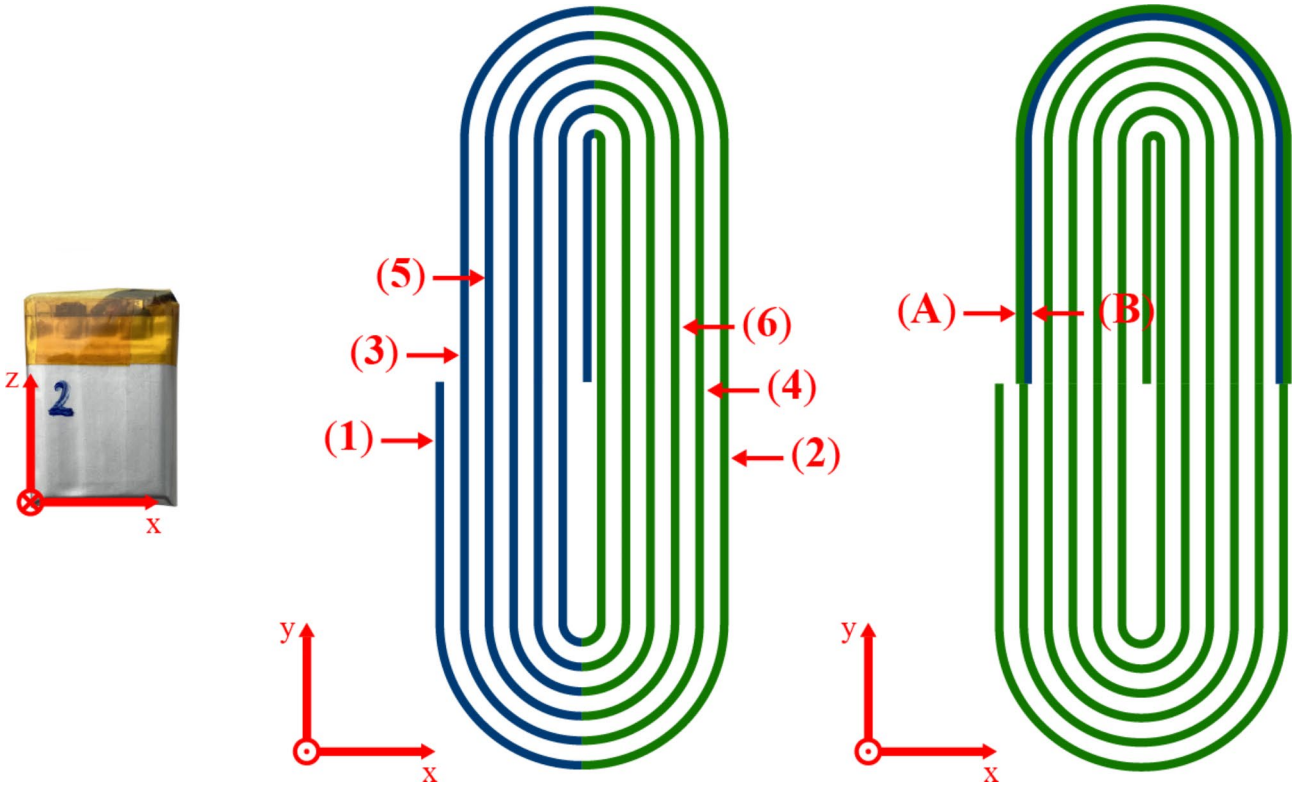


Fig. 3. Schematic region labelling explanation – individual layers are labelled by a number beginning at the outermost region; layers orientation (outwards, inwards) are labelled by a letter (**A**, **B**).

BIB, and SEM maintaining an argon atmosphere and preventing sample contamination and preserving sample integrity. Throughout the analysis, CleanConnect sample transfer was employed.

Results

The initial test cycle, conducted at 0.2 C, 0.5 C, and 1.0 C, revealed the reference battery's capacity to be 162.8 mAh, 157.5 mAh, and 151.2 mAh, respectively. The cell subjected to cycling exhibited capacities of 155.0 mAh, 150.2 mAh, and 144.2 mAh, respectively (Fig. 4C). Subsequently, the experiment subjected the battery to 100 cycles of 1 C load. Until cycle 42, the capacity demonstrated a gradual decline at a rate of approximately 0.15% per cycle. At this point, a more rapid capacity decline of about 0.6% per cycle became evident (see Fig. 4A and B). Furthermore, a decline in Coulombic efficiency (at the beginning was almost 100%) was observed in this phase. Ultimately, the battery reached the end of its cycle life after 59 cycles, accompanied by a 20% capacity loss. After completing 100 cycles, the total capacity loss reached 40%, to a final capacity of 86.5 mAh (compared to 144.2 mAh at the start of cycling). Finally, post-cycling test cycles performed at 0.2 C, 0.5 C, and 1.0 C revealed a capacity of 90.0 mAh, 68.9 mAh, and 45.8 mAh, respectively (Fig. 4C). This decrease in capacity was also accompanied by a significant drop in the discharge plateau. Notably, these test cycles were performed subsequently to the CT scan of cycled battery rather than immediately following the completion of the cycling process. Therefore, we assume that, meanwhile, in the cycled battery cell, a continuous degradation process took place. After the test was completed, a third cell from the same production series was subjected to the identical electrochemical testing. The result of this cycling was similar and rapid capacity degradation is therefore not a random event.

Figure 4D showcases the Nyquist diagram of the electrochemical impedance spectroscopy (EIS) data obtained before and after cycling, including the corresponding equivalent circuit model. The curves clearly show the significant changes that occurred because of cycling. The series electrochemical resistance (ESR) value, which initially measured 81 mΩ, increased to 167 mΩ after cycling. This change is associated with electrolyte decomposition, as was evident in the CT analysis of the battery swelling. Furthermore, this change is due to the increase in the solid electrolyte interphase (SEI) layer and along with the likely deposition of lithium on the electrode surface and the structural damage to the graphite in the anode layer, as evidenced by the combined changes in RSEI and the constant phase element CPE1. Before cycling, the RSEI value measured 19 mΩ, which subsequently increased to 442 mΩ post cycling. Simultaneously, there was an increase in the charge transfer resistance (RCT), which increased from 393 mΩ to 549 mΩ. This increase is related to the electrode corrugation, resulting in localised loss of contact and current overloading of the material in the contact area, which was additionally covered with a layer of decomposed electrolyte, as revealed by the CT and SEM analysis.

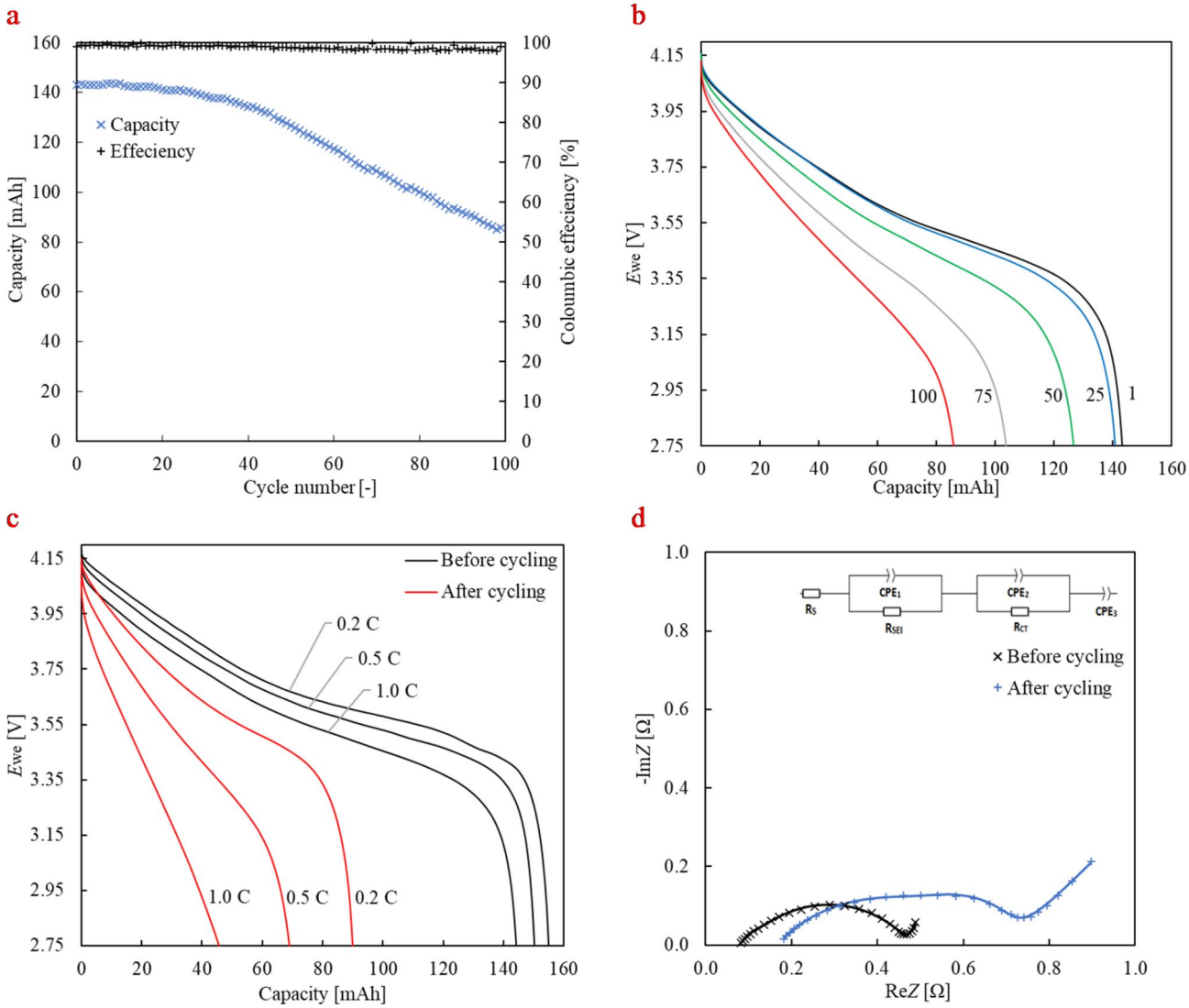


Fig. 4. Capacity (blue line) of the cell and Coloumbic efficiency (black line) after each cycle (***a***); discharge curves for selected cycle number (***b***); discharge curves for different C-rates before and after cycling (***c***); EIS before (black line) and after cycling (blue line) (***d***).

Utilization of space-filling helical trajectory enabled scanning of the cell on the whole cell level with sufficient resolution to distinguish components of the inner structure. Figure 5 presents a CT scan image of the cell before electrochemical cycling, depicting its internal structure. The cell comprises 12 anode and 13 cathode layers distinguished by the folds. The first outer active layer encountered is the anode marked as (1), followed by a single-coated cathode layer (2) positioned on the outer side, enveloping the anode. The second cathode layer commences in position (3), 8 mm below the initial beginning of the anode layer (1).

Consequently, this 8 mm section of the anode layer remains inactive. A notable gap can be observed within the cell's central region, resulting in a significant void. The electrodes tend to bend, creating two distinctive undulations or "waves" during cycling.

Following a series of 100 cycles, the battery experienced inflation by 29% in the x-axis (the thickness change was measured at the widest point). Comparing the tomographic cross-section of the cycled cell with the new cell (Fig. 6), it is evident that the bulged regions exhibit increased spatial separation. This bending induced by deformations has led to the emergence of new bulged regions situated at the lower side of the tomographic cross-section of the cell. Furthermore, the inter-electrode space reveals the presence of discernible material filling this void (Fig. 7).

During the cycling process, a fully charged reference cell was disassembled, and an optical inspection (Fig. 8) revealed a uniform lithiation pattern on the anode, indicated by its golden colour. However, the ends of the anode, where the cathode material is absent on the cathode side, remained black. Furthermore, slight discolouration of the separator is evident in the active regions, and the cathode material adhered to the separator in the bends of the cell edges. SEM analysis of the cathode cross-sections prepared using BIB revealed that the active material consisted of spherical particles with sizes up to 20 µm. The thickness of this active layer ranged from 55 to 60 µm,

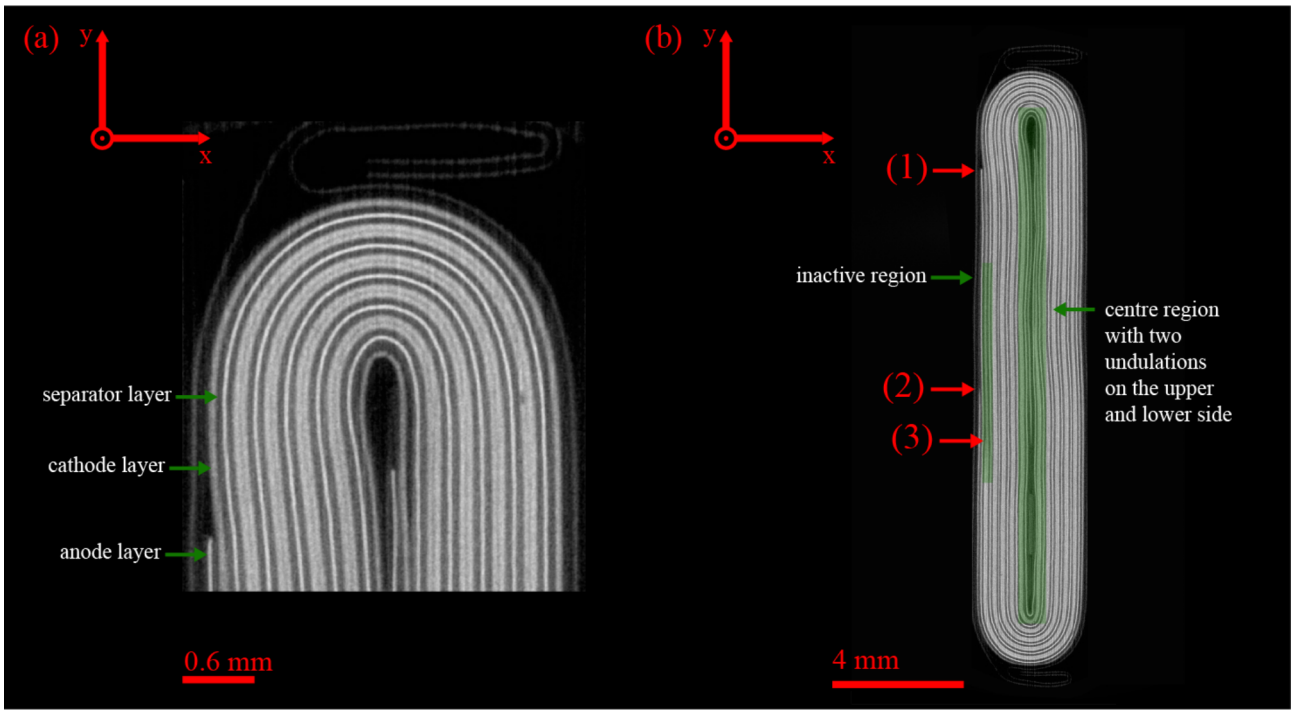


Fig. 5. Tomographic cross-section at z = 13 mm measured from the bottom of the battery cell) of whole cell level performed on Thermo Scientific HeliScan micro-CT system with resolution of 7.7 µm.

while the current collector is measured at approximately 12 µm. The overall thickness of the cathode measured 120 µm. In the case of the anode, the particles exhibited an oval shape in size up to 45 µm. The thickness of the active layer in the anode ranged from 55 to 65 µm, and the current collector was approximately 7.5 µm. The total thickness of the anode was 130 µm. Notably, the electrodes did not contain a surface layer, such as alumina).

Figure 8 presents different contrast exhibited by individual grains of the anode's active material. The EDS analysis shows the material is the same material – graphite. This difference may arise from varying degrees of lithiation, as the low-energy electron in-lens detectors are sensitive to conductivity. However, this assumption cannot be confirmed through EDS analysis. The cathode analysis confirmed the presence of NMC 532 as the electroactive material. Both electrodes also contained traces of fluorine, phosphorus and residual sulphur.

After analyzing the disassembled fully charged cell after cycling (Fig. 9), a noticeable observation is the incomplete lithiation of the anode in the cycled cell. The anode shows a lack of golden-coloured areas, indicating insufficient lithiation. However, dark regions can be identified, surrounded by bright, metallic shiny formations. The separator displays a more yellow-brown compared to its original appearance. At first view, there are no visually observable changes on the cathode. Furthermore, reduced delamination and adhesion to the separator are observed, indicating improved integrity.

A detailed CT scan shows material in the cavities (Fig. 10a, b). Optical inspection revealed this result from the lithium plating process (bright formations) taking place at the interface of the inactive region indicated by dark colour and the active region of the electrode (Fig. 10c, d). The inactive regions recorded by the optical microscope correlate to the cavities visible in the tomographic cross-section of the CT scan. The individual locations of these inactive regions can be correlated to the measured distances in the CT model. A BIB cross-section was prepared from the area on the active/inactive region boundary (Figs. 10e and 11).

The BIB cross-section SEM analysis of the anode exhibited graphite particle disintegration resulting from the lithium plating process (Fig. 11).

The individual graphite layers within graphite particles are tearing and separating apart due to the lithium growth. Some graphite layers lost contact with the grains, rendering them inactive. The height of the lithium layer on the surface reached up to 30 µm, causing a potential risk of short-circuiting. Considering the thickness of the separator is approximately 20 µm, this elevated lithium dendrite height increases the likelihood of puncturing the separator. Comparatively, the SEM/EDS analysis of the cathode cross-section indicated no notable changes in the internal structure composition or significant grain cracking (see supplementary data Fig. 4). However, the active regions were coated with a thick Cathode Electrolyte Interface (CEI) layer on the surface.

Furthermore, the anode and cathode surfaces were examined to assess their composition and structure across different regions. Figure 7 exhibits SEM images of the anode surface of the reference and aged cells in both the inactive and active areas within Region 4 A. Subsequently, Fig. 12 presents a corresponding analysis for the cathode in region 6 A. EDS analysis was conducted in all the areas mentioned above, and the results are summarized in Table 2 for the anode and Table 3 for the cathode.

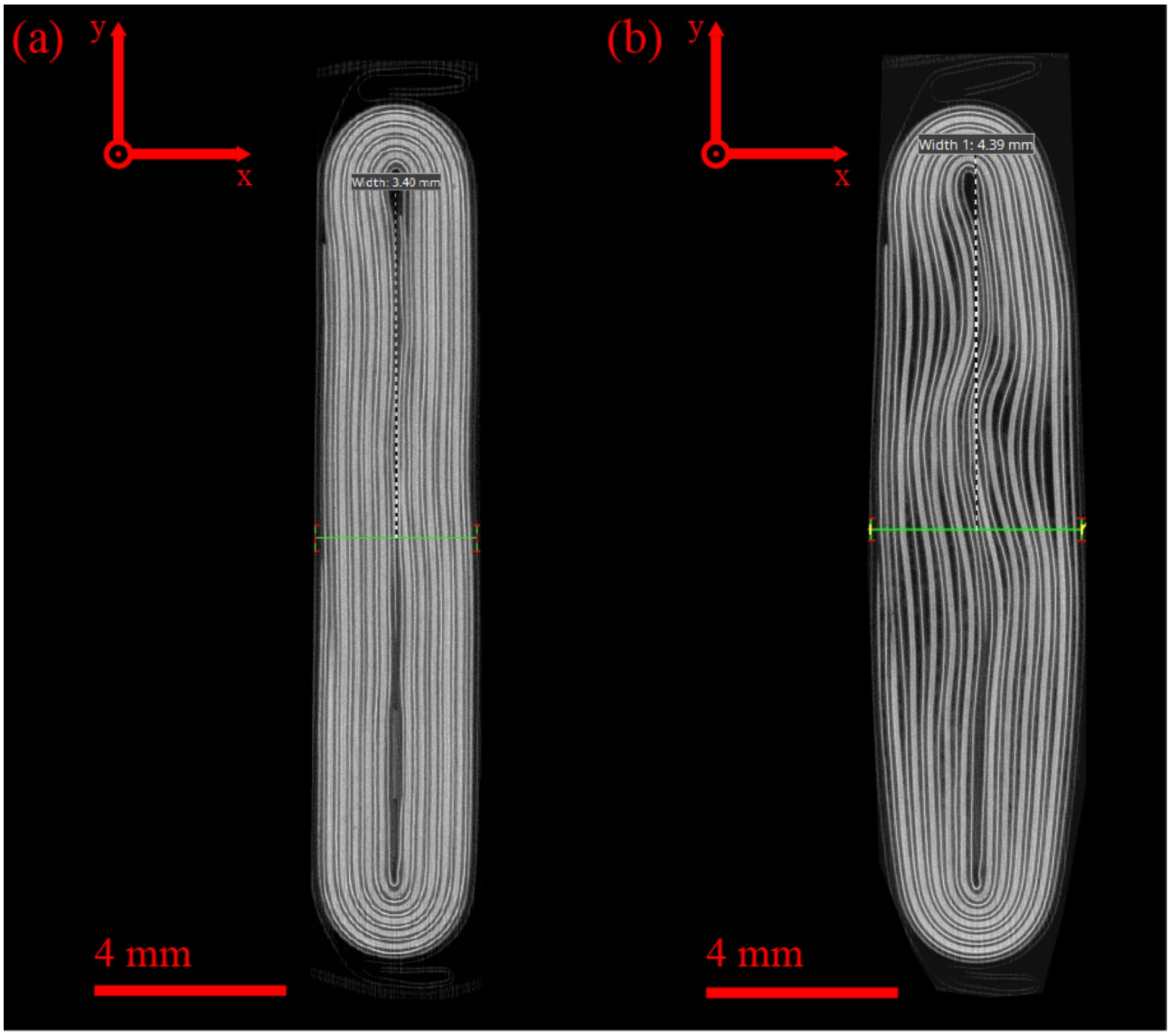


Fig. 6. Comparison of tomographic cross-sections (**a**) before and (**b**) after electrochemical cycling at z = 13 mm of whole cell level scan with resolution of 7.7 µm.

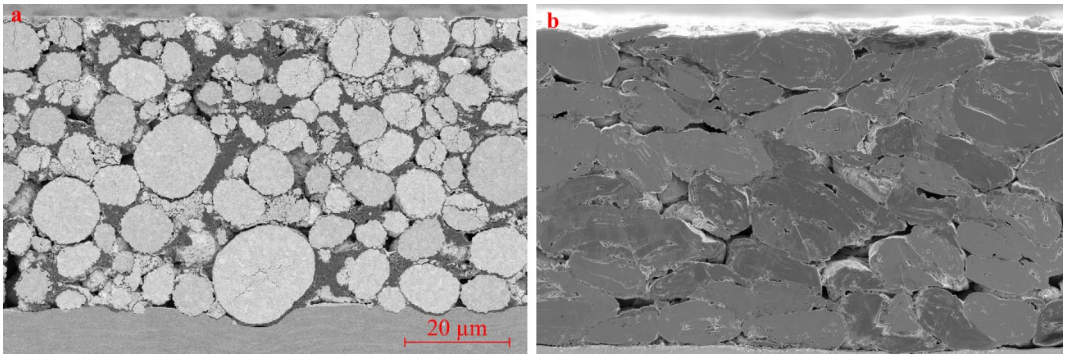


Fig. 7. SEM images of anode surface (region 4 A, HFW 100 µm) – reference cell (***a***); aged cell, inactive area (***b***); aged cell, active area (***c***).

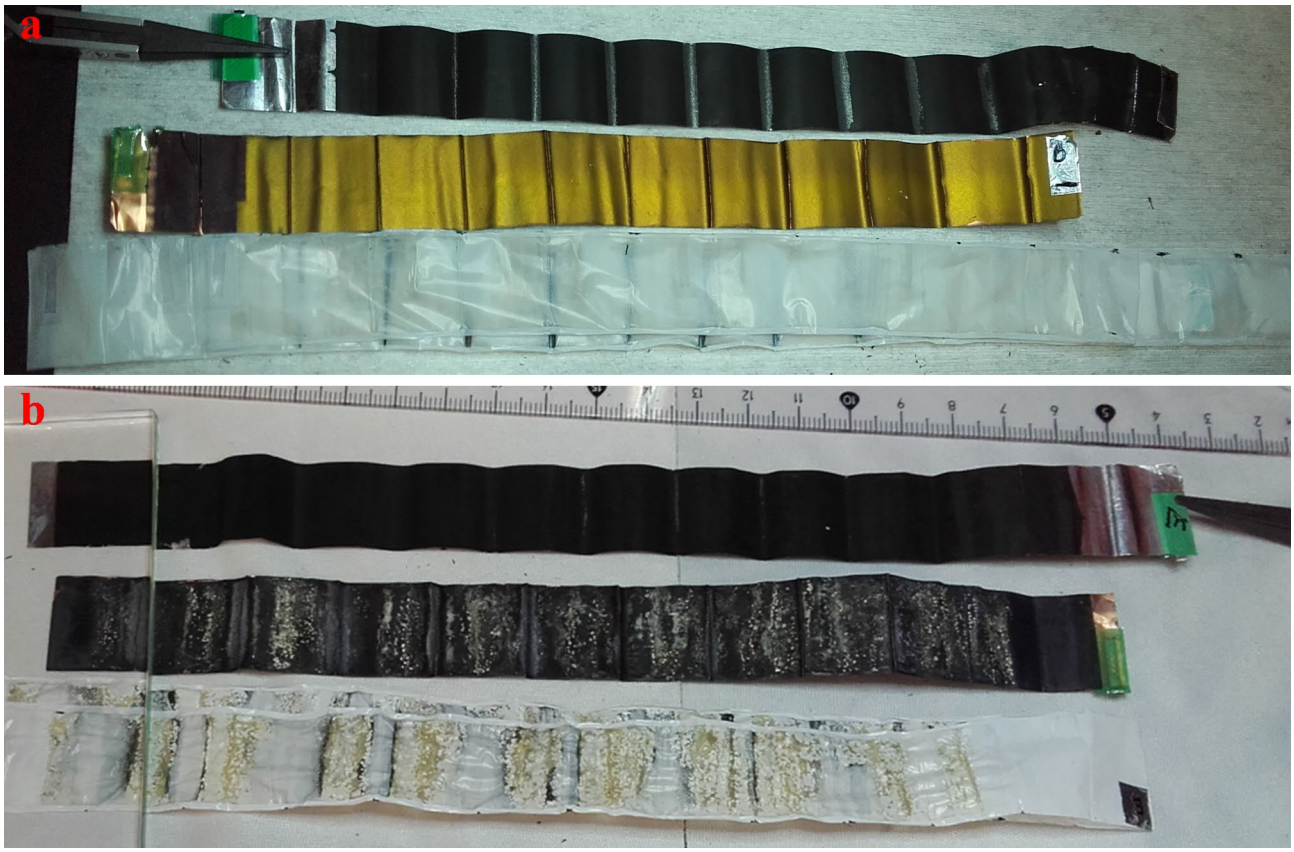


Fig. 8. SEM images of BIB cross-sections through reference cell electrodes (HFW 100 µm) – cathode region 6 A (***a***); anode, region 4 A (***b***).

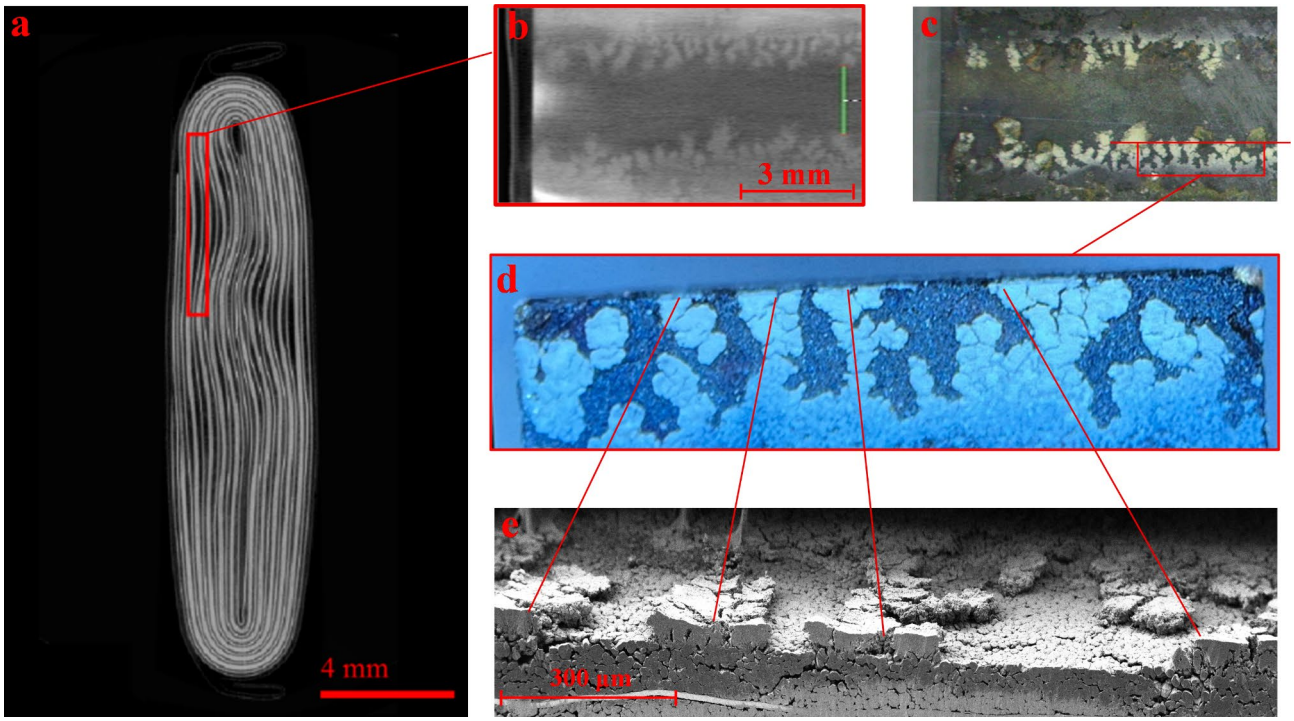


Fig. 9. Photo of disassembled cell; unrolled cathode, anode and separator (described from top to bottom); reference cell (***a***); cycled cell (***b***).

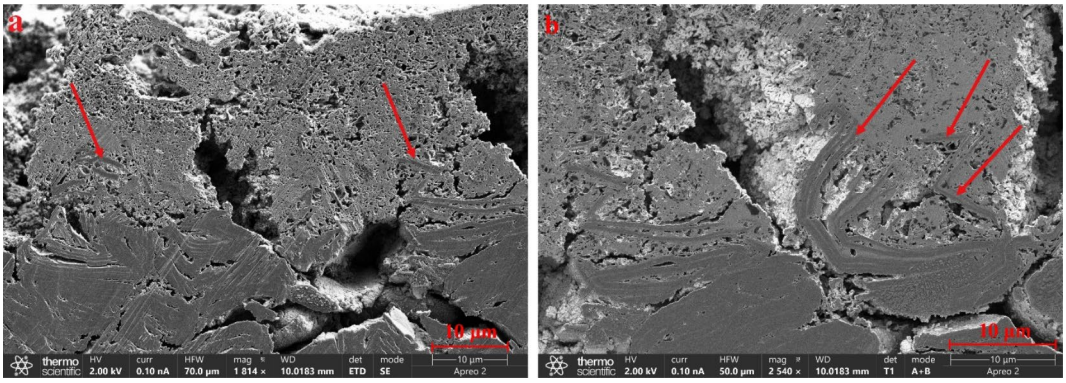


Fig. 10. Tomographic cross-section at z = 13 mm after cycling (***a***); tomographic section of anode surface, region 5 A (***b***); optical microscope image of region 5 A anode surface with marked area of interest (***c***); cut out area of interest, optical microscope image (***d***); SEM image of BIB cross-section through area of interest (***e***).

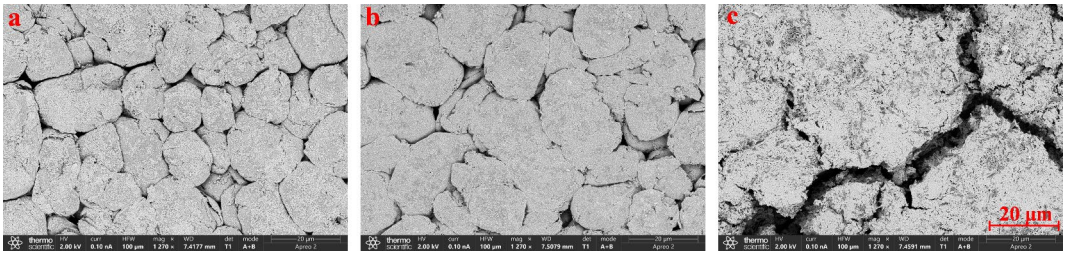


Fig. 11. SEM images of anode cross-section, cycled cell (Fig. 7e in detail). Lithium plated on the surface tearing graphite grains (a – HFW 70 µm; b – HFW 50 µm).

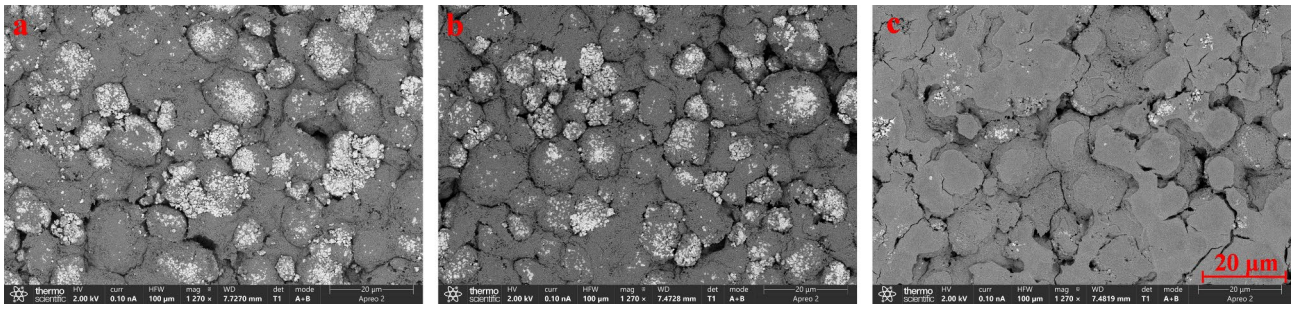


Fig. 12. SEM images of cathode surface (region 6 A, HFW 100 µm) – reference cell (**a**); aged cell, inactive area (**b**); aged cell, active area (**c**).

Anode	Atomic %		
Element	Reference	Aged inactive	Aged active
C	76.4	77.4	21.8
O	9.1	16.5	36.1
F	13.3	5	35.5
P	0.5	0.4	5.5
S	0.2	0.2	0.6

Table 2. Results of EDS analysis of anode surfaces, region 4 A.

Cathode	Atomic %		
Element	Reference	Aged inactive	Aged active
Ni	10.0	9.2	8.3
Mn	6.9	6.4	5.4
Co	4.2	3.8	3.5
O	33.8	34.9	34.6
C	27.2	30.3	25.1
F	17.3	14.8	21.8
P	0.4	0.3	0.9
S	0.1	0.1	0.3

Table 3. Results of EDS analysis of cathode surfaces, region 6 A.

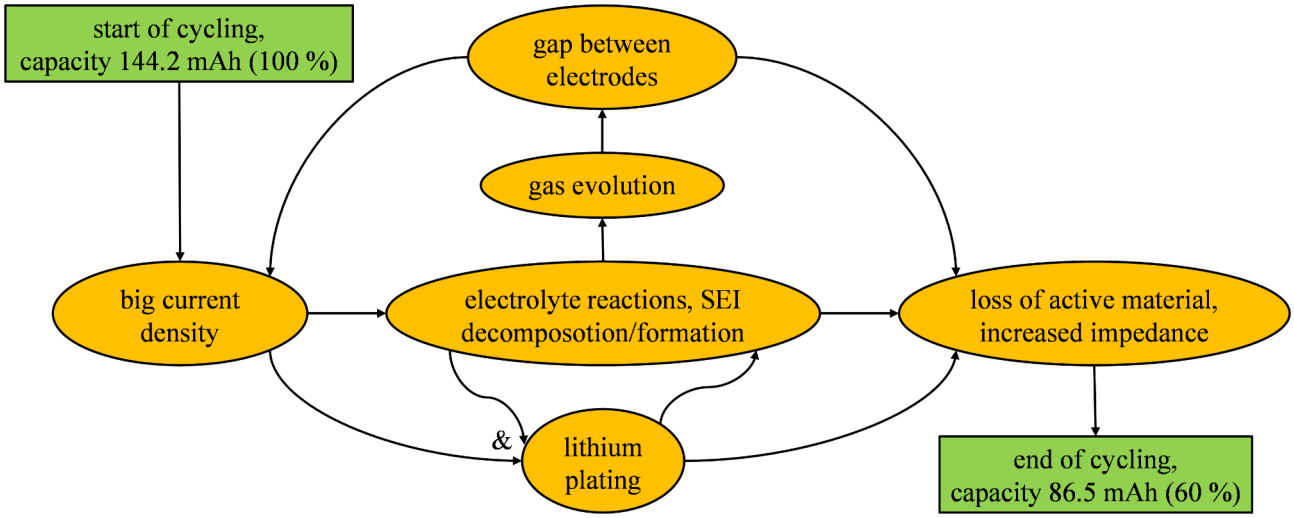


Fig. 13. Event diagram – the green rectangles show the cell status at the beginning and end of the cycling; yellow ellipsoids indicate a loop of events and degradation mechanisms leading to the final loss of capacity.

The SEM images reveal the surface structure of the reference electrode, which closely resembles the inactive region of the cycled cell for both the cathode and anode. However, EDS analysis exhibits changes in composition, specifically a decrease in fluorine and phosphorus content in these areas.

In contrast, the active regions shows a thick surface layer that overlaps over the active material grains, accompanied by a significant increase in fluorine and phosphorous content for both cathode and anode. Although EDS analysis does not directly detect lithium, elevated fluorine and phosphorus concentrations can indicate its presence on the anode side as intense electrolyte decomposition occurs there. The electrolyte decomposition is supported by high current density in active regions, which may explain the presence of these elements (fluorine and phosphorus) on the cathode side as well.

The trace amount of sulfur could be detected at a concentration of 0.1% in inactive areas and up to 0.3% in active areas. When it comes to concentrations that are this small, measurement errors must be considered. However, there is evidently a larger amount in the active areas of the electrode. The origin is probably electrolyte additives, which intensively decompose in active areas[31].

Discussion

The initial intention was to run 100 cycles, perform a CT scan, and then repeat the procedure until the battery reached the end of its life cycle. However, the battery exhibited faster degradation than expected and reached the end-of-life cycle after 59 cycles. This outcome could have been prevented. To describe the events leading up to the end of the life cycle, an event diagram in Fig. 13 was constructed, where there is derived and described every process.

Initially, a commercially available cell was procured that lacked mechanical fixation. It is well established that cycling at high C-rates requires the application of stack pressure to maintain optimal cell performance. However, as the objective of this study was to conduct a correlation analysis to investigate and accelerate degradation mechanisms, external pressure was not applied. Additionally, the commercial product datasheet provided no specific mention of pressure requirements. The initial micro-CT scan revealed a significant gap in the middle. Although the gap alone does not represent a significant problem, it permitted the electrodes to deform and bend into this gap, thereby increasing the distance between the electrodes. The cycled battery had slightly bent

electrodes at the beginning of cycling, which is probably why its capacity in the test cycles is slightly smaller than in the reference cell.

A 1 C cycling current was used to accelerate battery degradation. However, it was not intended to induce changes that would not occur under regular operation. Therefore, according to the datasheet, a value of 1 C was chosen, which is the maximum continuous load. However, as the BIB/SEM analysis of the anode has shown, it does not appear to be suited for such a current. The active layer is relatively thick with low porosity. In this case, there is a high risk of dendrite growth and excessive electrolyte decomposition.

During the operation, the electrodes underwent volumetric changes, and the electrolyte underwent side reactions that produced gas. Due to the lack of mechanical fixation, the gas inflated the cell, which increased the distance between the electrodes. This created vast inactive regions, leading to a significant loss of active area and a pronounced reduction in capacity. CT scans performed after cycling increased RSEI and RCT values, and electrode surface scans confirmed this outcome.

The manufacturer declares a maximum permissible current of 1 C derived from the current density. However, due to cell inflation, a large area became inactive. Since the current density is inversely proportional to the area, it exceeded the allowed maximum even though we maintained the current 1 C (which already seems disproportionately large). The elevated current density accelerates electrolyte decomposition at the electrode-electrolyte interface and induces the growth of a thick SEI layer, as confirmed in the active regions. This results in the consumption of lithium ions and loss of capacity. Moreover, it produces excessive gas, further inflating the cell, creating more inactive regions and increasing the current density. One event reinforces the other.

High current density can also disrupt the SEI layer, prompting the growth of a new SEI layer as confirmed by detecting the presence of higher levels of fluorine, phosphorus and sulfur. SEI layer disruption also facilitates a lithium plating process, which we observed. At the lithium-electrolyte interface, electrolyte deposition occurs excessively. Much of the lithium also becomes inactive. Lithium plating has been demonstrated to cause the graphite grains to break down and lose contact with the electrode, resulting in the loss of active material. Electroplated lithium together with decomposed electrolyte also reduces the porosity of the surface, thus reducing the ability of the electrode to work in this area.

All these factors contribute to rapid battery degradation and a significant reduction in the battery life cycle. Reviewing the event diagram shows that all the events pass through the big current density issue. A lower cycling current can be used, but there is a risk; however, due to the lack of mechanical fixation, the value could be too high after a certain number of cycles as inactive areas are formed. This problem can be easily prevented by incorporating mechanical fixation. One possible solution is to insert a solid core in the middle of the battery, around which the electrodes would be wound. External mechanical fixation would also enhance durability. In this case, the battery would probably withstand hundreds of cycles before another issue (e.g. particle cracking) becomes evident.

The battery was disassembled in a damaged state, with the anode lithiation level failing to reach the level required for graphite discolouration even at full charge. As a test, we attempted to charge and disassemble a battery of the same manufacturer, No. 304,050, with a capacity of 600 mAh (see Fig. 14). Due to its larger size, without mechanical fixation, only the edges of the electrodes exhibited good contact (golden areas), with a less active area in the middle, which would probably become completely inactive after a certain number of cycles. After that, a similar scenario to the cycled battery would probably follow.

Conclusion

Several analytical techniques were used to study the prismatic cell degradation mechanisms, making it possible to describe the degradation process and its causes related to the internal structure design in detail. The application of the methods was demonstrated on a commercially available cell with flexible packaging that was cycled at a high load of 1 C. During electrochemical cycling, the cell inflated, and its internal structure curled forming electrochemically inactive and active regions with high current density. These regions were then identified employing SEM/EDS and BIB together with IGTS in correlation with CT analysis. Thanks to the correlation of these methods, it was possible to determine a method to interpret the CT scan data, especially for identifying critical regions and areas with lithium plating or excessive electrolyte decomposition. In extreme cases, these destroy cells and may result in hazardous events. It was proven that CT scanning is a sufficient method, and evaluation can be performed without mechanically disassembling the cell. The created event diagram shows the sequence of detected events in a cycled cell that worsened as a spiral, with one event supporting the other. This was the reason for the 40% drop in capacity after 100 cycles.

Additionally, a procedure was proposed to disassemble the cell in a fully charged state. This approach is advantageous, as it allows observation of the anode's cross-section, studying the lithium plating process and observing disintegrated graphite grains in active regions with high current density. Finally, changes in the contrast of individual graphite grains on SEM imaging of the cross-section of the charged anode were observed. The origin of the phenomenon has yet to be confirmed. However, the presumption is that the degree of lithiation can be analyzed this way. Further investigation is necessary to understand this phenomenon.



Fig. 14. Anode surface of 600 mAh cell.

Data availability

The research data supporting the findings in this study are available at https://zenodo.org/records/13271360.

Received: 27 August 2024; Accepted: 24 October 2024
Published online: 18 November 2024

References

1. Lai, X. et al. Sorting, regrouping, and echelon utilization of the large-scale retired lithium batteries: A critical review. *Renew. Sustain. Energy Rev.* **146**, 111162. https://doi.org/10.1016/j.rser.2021.111162 (2021).
2. Sanguesa, J. A., Torres-Sanz, V., Garrido, P., Martinez, F. J. & Marquez-Barja, J. M. A review on electric vehicles: technologies and challenges. *Smart Cities* **4** (1), 372–404. https://doi.org/10.3390/smartcities4010022 (2021).
3. Halimah, P. N., Rahardian, S. & Budiman, B. A. Battery Cells for Electric Vehicles, (2019).
4. Pistoia, G. & Liaw, B. *Behaviour of Lithium-Ion Batteries in Electric Vehicles* https://doi.org/10.1007/978-3-319-69950-9 (2018).
5. Nur Halimah, P., Rahardian, S. & Budiman, B. A. Battery cells for electric vehicles, *Int. J. Sustain. Transport. Technol.* **2** (2), 54–57, https://doi.org/10.31427/IJSTT.2019.2.2.3 (2019).
6. Gerlitz, E., Greifenstein, M., Hofmann, J. & Fleischer, J. Analysis of the variety of lithium-ion battery modules and the challenges for an agile automated disassembly system. *Procedia CIRP* **96**, 175–180. https://doi.org/10.1016/j.procir.2021.01.071 (2021).
7. Ciez, R. E. & Whitacre, J. F. Comparison between cylindrical and prismatic lithium-ion cell costs using a process based cost model. *J. Power Sour.* **340**, 273–281. https://doi.org/10.1016/j.jpowsour.2016.11.054 (2017).
8. Liiv, O. Industrialization of lithium-ion prismatic battery cell for the automotive Industry. (2020)
9. Liu, Q. et al. Understanding undesirable anode lithium plating issues in lithium-ion batteries. *RSC Adv.* **6** (91), 88683–88700. https://doi.org/10.1039/C6RA19482F (2016).
10. Andrea, D. Battery management systems for large lithium-ion battery packs. (2010)
11. Withers, P. J. et al. X-ray computed tomography. *Nat. Rev. Methods Primers* **1** (1), 18. https://doi.org/10.1038/s43586-021-00015-4 (2021).
12. Pietsch, P. & Wood, V. X-Ray tomography for lithium ion battery research: A practical guide. *Annu. Rev. Mater. Res.* **47** (1), 451–479. https://doi.org/10.1146/annurev-matsci-070616-123957 (2017).
13. Gonzalez, J. et al. Three dimensional studies of particle failure in silicon based composite electrodes for lithium ion batteries. *J. Power Sour.* **269**, 334–343. https://doi.org/10.1016/j.jpowsour.2014.07.001 (2014).
14. Zhao, C. et al. Imaging of 3D morphological evolution of nanoporous silicon anode in lithium ion battery by X-ray nano-tomography. *Nano Energy* **52**, 381–390. https://doi.org/10.1016/j.nanoen.2018.08.009 (2018).
15. Lu, X. et al. 3D microstructure design of lithium-ion battery electrodes assisted by X-ray nano-computed tomography and modelling. *Nat Commun.* **11** (1), 2079. https://doi.org/10.1038/s41467-020-15811-x(2020).
16. Taiwo, O. O. et al. Investigating the evolving microstructure of lithium metal electrodes in 3D using X-ray computed tomography. *Phys. Chem. Chem. Phys.* **19** (33), 22111–22120. https://doi.org/10.1039/C7CP02872E (2017).

17. Pfrang, A. et al. Geometrical inhomogeneities as cause of mechanical failure in commercial 18650 lithium ion cells. *J. Electrochem. Soc.* **166** (15), A3745–A3752. https://doi.org/10.1149/2.0551914jes (2019).
18. Willenberg, L. et al. The development of jelly roll deformation in 18650 lithium-ion batteries at low state of charge. *J. Electrochem. Soc.* **167** (12), 120502. https://doi.org/10.1149/1945-7111/aba96d (2020).
19. Leung, C. L. A. et al. Correlative full field X-ray compton scattering imaging and X-ray computed tomography for in situ observation of lithium-ion batteries. *Mater. Today Energy* **31**, 101224. https://doi.org/10.1016/j.mtener.2022.101224 (2023).
20. Blazek, P. et al. Axially and radially inhomogeneous swelling in commercial 18650 lithium-ion battery cells. *J. Energy Storage* **52**, 104563. https://doi.org/10.1016/j.est.2022.104563 (2022).
21. Bond, T., Gauthier, R., Gasilov, S. & Dahn, J. R. In-Situ computed tomography of particle microcracking and electrode damage in cycled NMC622/Graphite pouch cell batteries. *J. Electrochem. Soc.* **169** (8), 080531. https://doi.org/10.1149/1945-7111/ac8a22 (2022).
22. Golozar, M., Gauvin, R. & Zaghib, K. In Situ and In operando techniques to study Li-ion and solid-state batteries: Micro to atomic level. *Inorganics* **9** (11), 85. https://doi.org/10.3390/inorganics9110085 (2021).
23. Li, Y., Guo, J., Pedersen, K., Gurevich, L. & Stroe, D. I. Recent health diagnosis methods for lithium-ion batteries, *Batteries* **8** (7), 72. https://doi.org/10.3390/batteries8070072 (2022).
24. Williard, N., Sood, B., Osterman, M. & Pecht, M. Disassembly methodology for conducting failure analysis on lithium–ion batteries, *J. Mater. Sci. Mater. Electron.* **22** (10), 1616–1630, https://doi.org/10.1007/s10854-011-0452-4 (2011).
25. Gholinia, A. et al. Coupled broad ion beam–scanning electron microscopy (BIB–SEM) for polishing and three dimensional (3D) serial section tomography (SST). *Ultramicroscopy* **214**, 112989. https://doi.org/10.1016/j.ultramic.2020.112989 (2020).
26. G. DESBOIS et al., Argon broad ion beam tomography in a cryogenic scanning electron microscope: a novel tool for the investigation of representative microstructures in sedimentary rocks containing pore fluid, *J Microsc.* **249** (3), 215–235. https://doi.org/10.1111/jmi.12011 (2013).
27. Waldmann, T. et al. Review—Post-Mortem analysis of aged lithium-ion batteries: disassembly methodology and physico-chemical analysis techniques. *J. Electrochem. Soc.* **163** (10), A2149–A2164. https://doi.org/10.1149/2.1211609jes (2016).
28. Kabir, M. M. & Demirocak, D. E. Degradation mechanisms in lithium-ion batteries: a state-of-the-art review, *Int. J. Energy Res.* **41** (14), 1963–1986. https://doi.org/10.1002/er.3762 (2017).
29. Burns, J. C., Stevens, D. A. & Dahn, J. R. In-Situ detection of lithium plating using high precision coulometry. *J. Electrochem. Soc.* **162** (6), A959–A964. https://doi.org/10.1149/2.0621506jes (2015).
30. Grimsmann, F. et al. Hysteresis and current dependence of the graphite anode color in a lithium-ion cell and analysis of lithium plating at the cell edge. *J. Energy Storage* **15**, 17–22. https://doi.org/10.1016/j.est.2017.10.015 (2018).
31. Tong, B. et al. Dec., Sulfur-containing compounds as electrolyte additives for lithium-ion batteries, *InfoMat* **3** (12), 1364–1392. https://doi.org/10.1002/inf2.12235 (2021).

Acknowledgements

This work was developed in cooperation with Thermo Fisher Scientific Brno. We acknowledge CzechNanoLab Research Infrastructure supported by MEYS CR (LM2018110). This work was supported by the Brno University of Technology specific graduate research grants CEITEC VUT/FEKT-J-22-7899 and FEKT-S-23-8286. This work was supported by the Brno University of Technology, Faculty of Mechanical Engineering grant FSI-S-23-8389. This work was supported by the state budget Technology agency of the Czech Republic under the National Centre of Competence Programme TN02000020. This work was supported by the project The Energy Conversion and Storage funded as project No CZ 02 01 01 00 22 008 0004617 by Programme Johannes Amos Comenius call Excellent Research. This work was supported by the project "The Energy Conversion and Storage", funded as project No. CZ.02.01.01/00/22_008/0004617 by Programme Johannes Amos Comenius, call Excellent Research.

Author contributions

Z.S. and O.K. proposed and developed the methods and protocols for the research, carried out the experiments and analyzed the data, managed and organized the data, including creating visual representations, wrote the initial draft of the manuscript, and coordinated the research project. J.B. reviewed published papers and wrote the initial draft of the manuscript.B.A. revised and edited the manuscript.P.B. developed the methods for the research and revised and edited the manuscript. T.Z. and T.K. formulated the research idea and goals, oversaw the research activity and managed the research project, secured financial support for the research, and revised and edited the manuscript.J.K. formulated the research idea and goals and secured financial support.

Declarations

Competing interests

The authors declare no competing interests.

Additional information

Supplementary Information The online version contains supplementary material available at https://doi.org/10.1038/s41598-024-77673-3.

Correspondence and requests for materials should be addressed to T.Z.

Reprints and permissions information is available at www.nature.com/reprints.

Publisher's note Springer Nature remains neutral with regard to jurisdictional claims in published maps and institutional affiliations.

Open Access This article is licensed under a Creative Commons Attribution-NonCommercial-NoDerivatives 4.0 International License, which permits any non-commercial use, sharing, distribution and reproduction in any medium or format, as long as you give appropriate credit to the original author(s) and the source, provide a link to the Creative Commons licence, and indicate if you modified the licensed material. You do not have permission under this licence to share adapted material derived from this article or parts of it. The images or other third party material in this article are included in the article's Creative Commons licence, unless indicated otherwise in a credit line to the material. If material is not included in the article's Creative Commons licence and your intended use is not permitted by statutory regulation or exceeds the permitted use, you will need to obtain permission directly from the copyright holder. To view a copy of this licence, visit http://creativecommons.org/licenses/by-nc-nd/4.0/.

© The Author(s) 2024